Inverse design of graphene-assisted metallodielectric grating and its applications in the perfect absorber and plasmonic third harmonic generation

SHUAI YU,[1] TIAN ZHANG,[1,*] XU HAN,[2] JIAN DAI,[1] AND KUN XU[1]

[1]*State Key Laboratory of Information Photonics and Optical Communications, Beijing University of Posts and Telecommunications, Beijing 100876, China*
[2]*2012 Lab, Huawei Technologies Co., Ltd, Beijing 100876, China*
*ztian@bupt.edu.cn

Abstract: In this article, we propose a graphene metamaterial coupled with metallodielectric grating (GMCMG) structures to achieve plasmon induced reflection effects in the reflection spectrums. In order to enhance the light-matter interaction in the graphene, the micro-genetic algorithm is applied in the performance optimization for the GMCMG. Due to the absorption enhancement of graphene and the inverse design of photonic structures, a perfect absorber and an efficient third harmonic generator are obtained by employing optimized GMCMG structures. Compared with previous works, our design scheme provides a simple and efficient method for the optimization of photonic devices and has significant applications in optical modulators, absorbers and sensors.

1. Introduction

Graphene, whose conductivity can be dynamically controlled by electrostatic doping or external electromagnetic field, has attracted a huge amount of attention [1–6]. Some graphene-based photonic devices have been proposed in recent years, such as graphene-assisted absorbers [3,4] and graphene-based nonlinear devices [5,6]. Recently, it has been experimentally demonstrated that graphene has strong nonlinear properties [6,7]. Due to the central symmetry of graphene, the second-order nonlinear capability of graphene vanishes within the dipole approximation [8]. On the other hand, a remarkably strong third harmonic generation (THG) can be processed by graphene in the infrared range [5]. The strong third harmonic response originates from the intraband electron transitions and the interactions between graphene and light [9]. However, it has been experimentally demonstrated that monolayer graphene absorbs only 2.3% of normal incidence light in the visible and near-infrared range, which limits its scope of applications [10]. Fortunately, the absorption can be improved by using the specific nanostructures to enhance the light-matter interaction in graphene [9]. Various nanostructures have been proposed to enhance it, including silicon waveguides [11], metal gratings [12], metamaterials [13], photonic crystal micro-cavities [14] and so on. Thus, based on the enhanced interaction between graphene and light, a high absorption rate and a high nonlinear conversion efficiency (CE) are expected to be achieved. It should be noted that the surface plasmon polarizations (SPPs), which can highly enhance the local field can be excited on the graphene under infrared light radiation [15] leading to its wide applications in enhancing the interaction of matter and light passing through it [16]. Based on this idea, several perfect absorbers have been implemented by using nanostructures, for example, gratings [17–20], metamaterials [21–23] and so on. Recently, it has been demonstrated that nanostructures with better performances can be designed by adjusting structure parameters with the help of the inverse design technology [24]. Combining the excitation of SPPs with the

inverse design, it is hopeful to further improve the optical absorption of graphene and the CE of THG in the graphene-assisted nanostructure.

With the advancement of computing capabilities, more and more algorithms have been introduced to help us efficiently design and optimize nanostructures, including gradient-based methods [25], gradient-free methods [26], and model-based methods [27,28]. As a representative method of the gradient-based methods, the adjoint variable method can optimize for the linear and nonlinear photonic devices [29,30], but it needs a physical background to derive the gradient of optimization objective. For the model-based methods, such as support vector machines and artificial neural networks, they try to establish the relationship between structure features (such as material properties) and optimization targets [27]. However, a lot of original data and labels are required to train the models, which need the consumption of computing resources and time [27]. Considering that our intention is to enhance the light-matter interaction in graphene or to improve the CE of THG, gradient-free methods, such as evolutionary algorithms, are appropriate due to their effectiveness and practicability [31]. However, it should be noted that although the evolutionary algorithms have been proved to be able to assist in the inverse design of nanostructures [31–34], they are time-consuming because they often require a large population consisted of many individuals to ensure the convergence of the algorithm [35]. Therefore, if the nanostructure is complicated or the simulation mesh is high-precision (such as the simulation of graphene), then, the optimization of the nanostructure is time-consuming and even not feasible. In order to solve this issue, some lightweight evolutionary algorithms, for example, micro genetic algorithm (μ-GA) [35–37], micro particle swarm optimization [38] and micro differential evolution algorithm [39] are proposed to reduce optimization time by maintaining a small population. Among the small population algorithms, the μ-GA can reduce the size of the population effectively and ensure the optimization performance at the same time [40,41]. Thus, the μ-GA is employed for the optimizations of nanostructures in this article.

In this article, three different graphene metamaterials coupled with metallodielectric grating (GMCMG) structures are proposed to achieve a perfect absorber and enhance the CE of THG based on the inverse design technology. In section 2, three GMCMG structures consisted of single-layer and double-layer graphene are compared to select the most appropriate one, which is hopeful to provide a perfect absorption peak in the infrared range. It is interesting to observe that the plasmon induced reflection (PIR) effects emerge in the reflection spectrums of the GMCMG structures. The PIR effect is a similar effect to the plasmon induced transparency (PIT) effect, which is a plasmonic analog of the electromagnetically induced transparency (EIT) effect and can provide a narrow peak in a wide spectrum band [42]. The difference is that the PIR effect occurs in the reflection spectrum. Both of them can be explained by employing classical bright and dark mode theory [43,44]. The PIR effect has been theoretically analyzed and experimentally realized in metamaterials [45]. It plays a significant role in optical switching and signal processing in plasmonic circuits [46]. By adjusting the chemical potential of graphene and critical structure parameters, we analyze the mechanism of the PIR effect. In section 3, the μ-GA is used to optimize the GMCMG structure. Due to the enhancement of the light-matter interaction in graphene, a perfect absorption peak (0.9956) and a high CE of THG are obtained by employing the optimized GMCMG structures.

2. Structure design and simulation results

Different GMCMG structures with single-layer graphene and double-layer graphene are designed to make a comparison. As shown in Fig. 1(a), first of all, we design a simple GMCMG structure composed of a single graphene nanoribbons grating (GNG), a dielectric interlayer, a gold grating and a dielectric waveguide. The refractive index of the dielectric interlayer and the dielectric waveguide are set as 1.57 and 1.95, respectively, for simplicity without loss of generality [43]. The thickness of the dielectric waveguide D_1 is set as 500 nm. The gold grating is placed

periodically in the x direction and extends to infinity in the z direction. The thickness of the gold grating D_2 is set as 150 nm. The period of gold grating L_{per} and the width of the slit L_{gap} are 4000 nm and 250 nm, respectively. The period of the GNG L_{gper} is set to 1/10 of the Au grating L_{per}, and the duty cycle L_g / L_{gper} is 50%. The thickness of the interlayer D_{int} is 500 nm. The permittivity of gold is calculated by using the Drude model [47]:

$$\varepsilon_{Au}(\lambda) = 1 - [(\frac{\lambda_p}{\lambda} + i\gamma)\frac{\lambda_p}{\lambda}]^{-1} \tag{1}$$

where λ_p (=1.5895×10^{-7} m) indicates the plasma wavelength and γ (=0.0077) indicates the metal loss. In the simulation, the thickness of monolayer graphene is set as 0.34 nm. The conductivity of graphene is modeled by the Kubo formula [48]:

$$\sigma_g = i\frac{e^2 k_B T}{\pi\hbar^2(\omega + i\tau^{-1})}\left[\frac{\mu_c}{k_B T} + 2\ln\left(\exp\left(-\frac{\mu_c}{k_B T}\right) + 1\right)\right]$$
$$+ i\frac{e^2}{4\pi\hbar}\ln\left[\frac{2|\mu_c| - \hbar(\omega + i\tau^{-1})}{2|\mu_c| + \hbar(\omega + i\tau^{-1})}\right] \tag{2}$$

where e, k_B, T (=300 K), $\hbar$, τ (=0.5 ps), ω and μ_c indicate the electron charge, the Boltzmann's constant, temperature, the reduced Planck's constant, relaxation time, angular frequency and chemical potential, respectively. In the mid-infrared range, considering $\mu_c >> k_B T$, the simplified conductivity of single-layer graphene can be expressed as [48]:

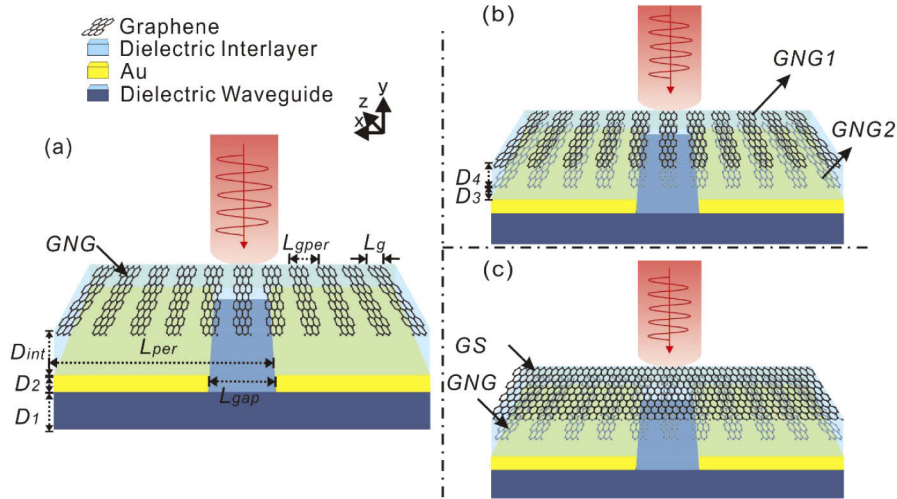$$\sigma_{fg} = i\frac{e^2 \mu_c}{\pi\hbar^2(\omega + i\tau^{-1})} \tag{3}$$

Fig. 1. (a) Schematic diagram of the GMCMG structure with single layer graphene nanoribbons grating (GNG). (b) Schematic diagram of the GMCMG structure with a double-layer GNG. (c) Schematic diagram of the GMCMG structure with a hybrid graphene structure composed of a GNG and a graphene sheet (GS).

In addition to the GMCMG structure with single-layer graphene, the GMCMG structures with double-layer graphene have also been investigated. As shown in Fig. 1(b), another GNG labeled as GNG2 is added into the interlayer between gold grating and GNG1. What's more, we also try to investigate the influences of the different types of graphene layers in the GMCMG

structure. As illustrated in Fig. 1(c), (a) hybrid GMCMG structure, whose upper graphene layer is a graphene sheet (GS) and lower graphene layer is a GNG, is proposed. The distance between the GS and GNG is set as $D_4 = 20$ nm, while that between the GNG and gold grating is set as $D_3 = 650$ nm. The other structural parameters are set the same as those of the GMCMG structure shown in Fig. 1(a). It should be noted that these structures are realizable based on the current nano-fabrication technology [49,50]. In this article, all the GMCMG structures shown in Fig. 1 are simulated by using the 2D finite-difference time-domain (FDTD) method. In order to balance the computational accuracy and simulation consumption, the mesh inside the graphene region is kept as 0.17 nm, which is small enough to ensure the numerical convergence [12].

When TM polarized light illuminates on the GMCMG structure with a single GNG, the simulated spectra are shown in Fig. 2(a). The chemical potential of the graphene is set as $\mu_c = 0.65$ eV. It can be found that three dips, which are labeled as A, B and C, emerge in the reflection spectrum. Comparing with the absorption peak of the structure without metal grating (green dashed line), the absorption rate at the wavelength corresponding to dip C is enhanced significantly, leading to stronger interaction between the incident light and the graphene. It is interesting to observe that the PIR effect, which is manifested as a reflection peak located between two reflection dips, appears in the reflection spectrum. The appearance of the PIR effect is related to the destructive interference between the SPPs mode excited on graphene and the hybrid mode in the nearby medium [51–53]. As shown in Fig. 2(b), when the chemical potential of graphene is increased from 0.63 eV to 0.67 eV, the reflection dip C shows an obvious blue-shift, while the reflection dips A and B are stable. The 2D FDTD simulation results shown in Fig. 2(c) also confirm this phenomenon. As illustrated in Fig. 2(c), the absorption peak originated from the excitation of SPPs on the graphene blue-shifts proportionally as the chemical potential of the graphene increases from 0.63 eV to 0.67 eV. In order to get further insight into the physical mechanisms of the reflection characteristics, the spatial magnetic field distributions of the reflection dips A, B and C are shown in Fig. 2(a). Here, the field distributions near the GNG are magnified prominently. It can be found that the hybrid mode consisted of SPPs mode, cavity mode and TM_0 guide mode resonance confined in interlayer form the reflection dip A [12]. And the excitation of the cavity mode in the slit can be demonstrated by using the phase equation [54]:

$$\varphi_{12} + \varphi_{23} + kD_2 = 2n\pi(n = 1, 2, \ldots, N) \tag{4}$$

where the phases φ_{12} and φ_{23} are caused by the reflection in the slits of gold grating, and k is the complex wave vector in the slit. The excitement SPPs mode on the surface between the gold grating and dielectric interlayer can be explained by the dispersion equation [51]:

$$k_{spp} = -n\frac{2\pi}{L_{per}} = -\frac{2\pi}{\lambda}\sqrt{\frac{n_{Au}^2(\omega)\varepsilon}{n_{Au}^2(\omega) + \varepsilon}} \tag{5}$$

where λ is the wavelength of incident light and ε is the relative permittivity of the interlayer closed to the surfaces of gold grating and n represents the diffraction order. It is worth noting that because the thickness of the gold grating is 150 nm, it can only support the zero-order vertical cavity mode and the characteristics of the cavity mode are not very clear to discern here [12]. As shown in the field distribution of the reflection dip B, we can find a hybrid mode consisted of cavity mode and the guide mode resonance confined in the dielectric waveguide. For the field distributions of the reflection dip C, a strong localized surface plasmon polaritons (LSPPs) is excited on the GNG. The resonant wavelength of the GNG λ_{res} can be calculated from the quasi-static analysis [55]:

$$\lambda_{res} \approx \frac{2\pi c\hbar}{e}\sqrt{\frac{\eta(n_0^2 + n_1^2)\varepsilon_0 L_g}{2\mu_c}} \tag{6}$$

where c, ε_0 represent the light speed and vacuum dielectric constant of graphene, respectively.

The n_0 (=1) is the refractive index of air and the n_1 (=1.57) is the refractive index of the dielectric layer beneath the GNG. The constant η (=0.52) is a fitting parameter that is deduced from the simulation results. As shown in the insert of Fig. 2(a), the simulated results of the wavelengths of reflection dip C fit well with the theoretically calculated ones from Eq. (6). The wavelength of reflection dip C becomes shorter as the Fermi level of the GNG increases or as the graphene nanoribbon's width decreases. This provides another point of evidence that the reflection dip C is attributed to the LSPPs mode excited on the GNG. It is noteworthy that the hybrid mode excited nearby the gold grating has nothing to do with the chemical potential of graphene, thus the central wavelengths of the reflection dip A and B are stable as the chemical potential of graphene increases from 0.63 eV to 0.67 eV [shown in Fig. 2(b)]. The formation of the PIR window can
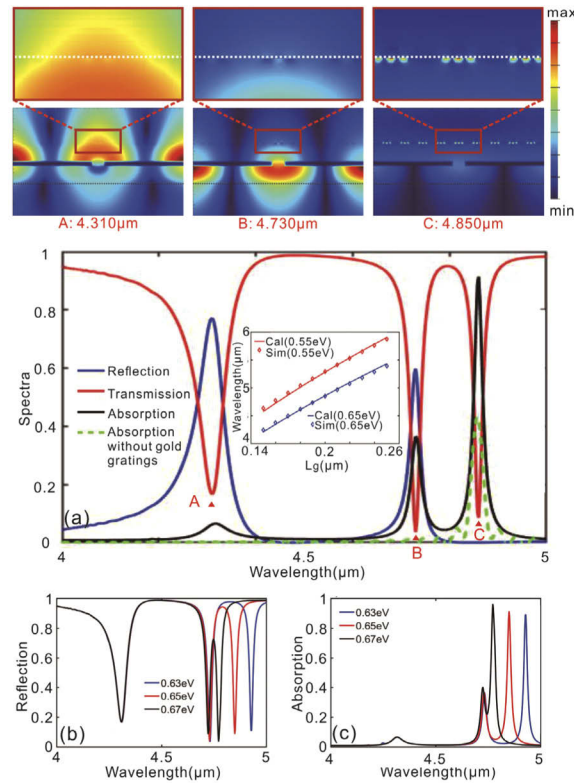

Fig. 2. (a) When plane wave vertically incident on the structures, the blue solid line, red solid line, and black solid line represent the simulated reflection, transmission and absorption spectra of the GMCMG structure with a GNG, respectively. The green dashed line represents the absorption spectrum of the GMCMG structure without gold gratings. The upper three panels represent the spatial magnetic field distributions corresponding to the reflection dips A (λ=4.310 μm), B (λ=4.730 μm) and C (λ=4.850 μm), respectively. The black dashed line in the spatial magnetic field distributions figure is the lower boundary of the structure, and the white dashed line in the enlarged picture is the position of the graphene. The insert shows the theoretically calculated results (Cal) and simulated results (Sim) for the resonant wavelength of the LSPPs modes versus different L_g. (b) The reflection spectrums of the simple GMCMG structure for different chemical potentials of graphene (blue solid line for μ_c=0.63 eV, red solid line for μ_c=0.65 eV and black solid line for μ_c=0.67 eV). (c) The absorption spectrums of the simple GMCMG structure for different chemical potentials of graphene (blue solid line for μ_c=0.63 eV, red solid line for μ_c=0.65 eV and black solid line for μ_c=0.67 eV).

also be explained by using classic bright-dark mode coupling mechanism, which has been widely used to describe PIT effects [12,56]. Concretely, the hybrid mode excited nearby the gold grating acts as the bright mode, while the LSPPs mode excited on the graphene can be regarded as the dark mode here due to its excitation is restricted by the bright mode. In addition, as shown in Fig. 2(c), the height of the absorption peak is improved when the chemical potential of GNG increases from 0.63 eV to 0.67 eV, which indicates that a perfect absorber (A≈1) is expected to be achieved by adjusting the chemical potential of graphene and the structure parameters of the GMCMG.
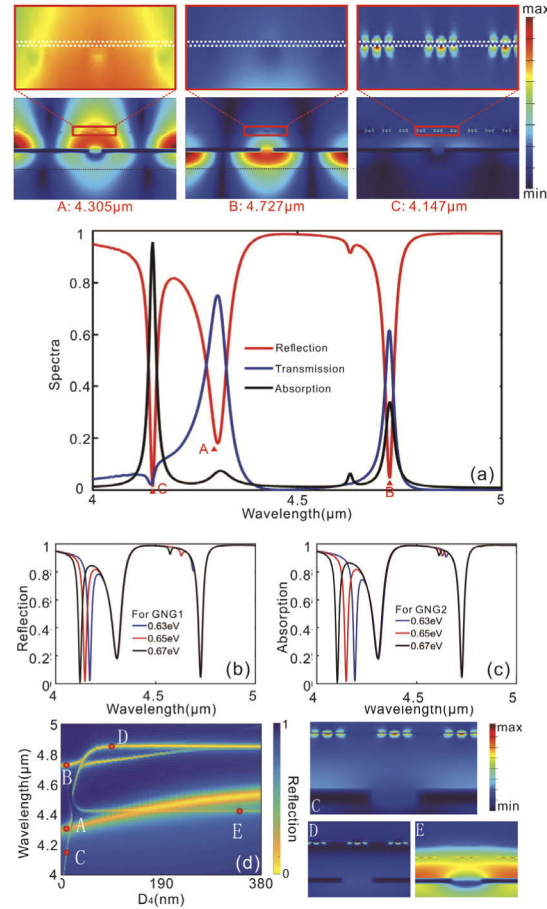

Fig. 3. (a) When plane wave vertically incident on the structures, the blue solid line, red solid line, and black solid line represent the simulated reflection, transmission and absorption spectra of the GMCMG structure with a double-layer GNG, respectively. The upper three panels represent the spatial magnetic field distributions corresponding to the reflection dips A (λ=4.305 μm), B (λ=4.727 μm) and C (λ=4.147 μm), respectively. (b) The reflection spectrums of the complex GMCMG structure for different chemical potentials of GNG1 (blue solid line for μ_c=0.63 eV, red solid line for μ_c=0.65 eV and black solid line for μ_c=0.67 eV). (c) The absorption spectrums of the complex GMCMG structure for different chemical potentials of GNG2 (blue solid line for μ_c=0.63 eV, red solid line for μ_c=0.65 eV and black solid line for μ_c=0.67 eV). (d) Simulated reflectance contour plots of the complex GMCMG structure versus D_4 and wavelength. The spatial magnetic field distributions corresponding to the reflection dips C, D and E.

For the complex GMCMG structure composed of the double-layer GNG, the simulated spectra are shown in Fig. 3(a). Here, the chemical potentials of the GNG1 and GNG2 are set as 0.65eV. The spatial magnetic field distributions of reflection dips A, B and C are also shown in Fig. 3(a) and the field distributions near the graphene layers are magnified prominently. In comparison to the simulation results shown in Fig. 2(a), reflection dips A and B still exist in the reflection spectrum, which indicates that these dips are irrelevant to the GNGs. It is interesting to see that a new dip labeled C emerges in the reflection spectrum. The PIR effect whose component dips are A and C can also be found in the reflection spectrum. From the spatial magnetic field distributions of the reflection dip C, we can find that on both GNG1 and GNG2, a strong LSPPs mode has been excited. And the close-range (20 nm) excitation causes coupling between two LSPPs modes, which greatly enhances the absorption of light as the black solid line in Fig. 3(a) shows. Thus, for both GNG1 and GNG2, the increase in the chemical potential will cause the equivalent refractive index of the SPPs modes supported on graphene to increase, leading to the decrease of the equivalent wavelength of SPPs mode. As a result, the reflection dip C blue shifts. [Figs. 3(b) and 3(c)]. In addition, we consider the influence of the distance between two GNGs (D_4) on the PIR effect, and the simulation results are shown in Fig. 3(d). The spatial magnetic field distributions, corresponding to the reflection dips C, D and E are also illustrated in Fig. 3(d). The bright regions in this figure correspond to the reflection dips in the reflection spectrums. The marked points in Fig. 3(d) are representative reflection dips, among which points A, B and C are the dips mentioned in Fig. 3(a). The reflection dips C, D and E are caused by the SPPs excited on GNGs. From their spatial magnetic field distributions, it can be found that dip C is caused by the SPPs excited on both the upper and lower GNGs. Dips D and E relate to the SPPs excited on GNG1 and GNG2, respectively. The reflection dip C only emerges when the distance between the GNGs is smaller than 40 nm, while reflection dips D and E emerge after D_4 gets larger. In other words, the strong coupling between the two LSPPs modes occurs when D_4 is smaller than 40 nm. Apparently, the adjustment of the key structure parameters also affects the excitation modes in the complex GMCMG structure.

For the hybrid GMCMG [Fig. 1(c)] whose upper graphene layer is a GS and lower graphene layer is a GNG, the FDTD simulated spectra are shown in Fig. 4(a). Here, the chemical potentials of the GS and GNG are set as 0.65 eV. As expected, the reflection dips A and B still exist in the reflection spectrum. It's remarkable that two PIR effects appear in the reflection spectrum. From the absorption spectrum, we can attribute the generation of reflection dips C, D and E to the corresponding absorption peaks. We assume the reasons for the formation of the absorption peaks are the excitation of the SPPs on the GNG or GS. In order to validate this assumption, the spatial magnetic field distributions of reflection dips C, D and E are shown in Fig. 4(a). It can be found that there are SPPs on the surface of the graphene and there are spatial couplings between the SPPs on the GNG and those on the GS. Different from the results in Fig. 3, they can be interpreted as the coupling effect between the LSPPs excited on the GNG and the delocalized surface plasmon polaritons (DSPPs) excited on the GS [57]. The LSPPs are non-propagate modes, while the DSPPs can propagate along the GS. It should be noted that the DSPPs are not excited by the incident light because the phase matching equation is not satisfied. The DSPPs are coupled by the LSPPs on the GNG because of the strong modal overlap between the two SPPs modes. Consequently, as shown in Fig. 4(b) and Fig. 4(c), when the potential chemical of graphene increases from 0.63 eV to 0.67 eV, the reflection dips C, D and E exhibit obvious blue shifts, while the other two reflection dips A and B are stable. Obviously, a dynamically tunable double PIR effect is achieved in this GMCMG structure. Similarly, we also consider the influence of the distance between the GNG and GS (D_4) on the reflection spectrums, and the simulation results are shown in Fig. 4(d), in which marked reflection dips A, B, C, D and E correspond to the reflection dips in Fig. 4(a). The spatial magnetic field distributions near the graphene layers corresponding to the reflection dips labeled F, G and H are also illustrated

in Fig. 4(d). Reflection dips A and B correspond to the modes excited surrounding the gold grating, which can be also found in Fig. 3(d). When D_4 is larger than 50 nm, the reflection dip H becomes stable, which is related to the SPPs mode excited on the GNG, as demonstrated by the spatial magnetic field distribution. By contrast, as can be found in Fig. 4(d), the reason for the reflection dip G is related to the DSPPs mode excited on the GS. It is interesting to see the spatial magnetic field distribution of reflection dip F simultaneously concentrated on both GNG and GS. It demonstrates the formation of LSPP-DSPP polaritons. As D_1 decreases, a new reflection
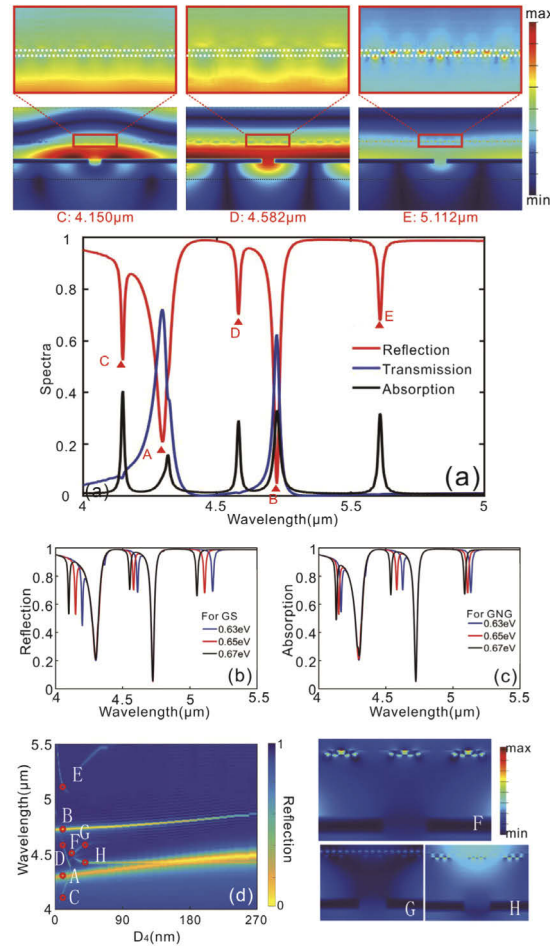

Fig. 4. (a) When plane wave vertically incident on the structures, the blue solid line, red solid line, and black solid line represent the simulated reflection, transmission and absorption spectra of the GMCMG structure whose upper graphene layer is a GS and lower graphene layer is a GNG, respectively. The upper three panels represent the spatial magnetic field distributions corresponding to the reflection dips C (λ=4.150 µm), D (λ=4.582 µm) and E (λ=5.112 µm), respectively. (b) The reflection spectrums of the hybrid GMCMG structure for different chemical potentials of GS (blue solid line for μ_c=0.63 eV, red solid line for μ_c=0.65 eV and black solid line for μ_c=0.67 eV). (c) The absorption spectrums of the hybrid GMCMG structure for different chemical potentials of GNG (blue solid line for μ_c=0.63 eV, red solid line for μ_c=0.65 eV and black solid line for μ_c=0.67 eV). (d) Simulated reflectance contour plots of the hybrid GMCMG structure versus D_4 and wavelength. The spatial magnetic field distributions corresponding to the labeled points F, G and H.

dip with marked point E appears at a larger wavelength, which attributes to lower order DSPP resonance. The gradual appearance of the modes supported by the GS is due to the increasing excitation efficiency of the GNG as the distance between the two graphene layers decreases. The LSPP-NSPP polaritons are enhanced because of the greater modal overlap between two types of SPPs.

3.   Applications based on inverse design

3.1.   Perfect absorber

As shown by the simulation results in section 2, both the GMCMG structures with a single-layer GNG and double-layer GNG can provide a considerable high absorption peak. Considering the complexity in the simulation and difficulty in fabrication, we select the GMCMG structure with a single GNG for further optimization in this section. Notably, the optimization method applied in the following content is also available for the optimization of other similar nanostructures like the structures in Fig. 1(b) and Fig. 1(c). As mentioned above, we can regulate its absorption peak by optimizing the structure parameters of the GMCMG. The genetic algorithm (GA) is introduced to the optimization process because it is highly effective in handling the problem with a high dimensional variable search space [35]. However, a single simulation of our structure needs nearly half an hour to reach convergence on a server with 56 threads [Intel Xeon CPU E5-2680 v4 @ 2.40 GHz]. Considering that traditional GAs will consume much time and a lot of computing resources, we will use the μ-GA to optimize the GMCMG structure. Every generation in the μ-GA includes five individuals, one of which is directly taken from the previous generation, in other words, only four FDTD simulations are needed in each generation. We save the structure parameters and fitnesses of the previous individuals to reduce the total calculation time by avoiding repeated simulations. The flowchart of the μ-GA we used is illustrated in Fig. 5. Each individual in the population is expressed as **P** containing five structure parameters:

$$\mathbf{P} = [D_1, D_2, L_{per}, D_{int}, L_{gap}] \tag{7}$$

The chemical potential of graphene in the GMCMG structure is fixed at 0.65 eV. The fitness of the μ-GA is the absorption peak caused by the LSPPs mode excited on the GNG [i.e. the absorption peak C in Fig. 2(a)]. The initial fitness for **P** = [0.5 μm, 0.15 μm, 4 μm, 0.5 μm, 0.25 μm] is 0.913. We set the domains of structure parameters as D_1 (0.4 μm - 0.6μm), D_2 (0.1 μm - 0.2 μm), L_{per} (3.6 μm - 4.4 μm), D_{int} (0.4 μm - 0.8 μm), L_{gap} (0.2 μm - 0.3 μm). Limited by the mesh setting of the FDTD simulation, the precision of the first structure parameter D_1 is set as 0.001 μm, and the precisions of the other structure parameters are set as 0.01 μm. The other four individuals in the initial generation are randomly generated from the parameter space. In each generation, the elite individual whose fitness (absorption peak) is highest is selected to directly be copied into the next generation, while the individual with the lowest fitness is eliminated. The other three individuals and the elite individual are randomly paired. Each pair generates two child individuals based on the single-point crossover method [58]. The four child individuals and the elite make up the next generation. If the best fitness no further increases for five consecutive generations, the four individuals except the elite are updated, that is, randomly selected in the parameter space. It should be noted that as enough diversity has already been introduced, the mutation operator in the traditional GA is not necessary for the μ-GA [35]. The evolution of the absorption peak for the GMCMG structure in each generation is shown in Fig. 6. It can be found that the fitness presents ladder form rise, which indicates the μ-GA is convergent. After 300 generations, the best absorption peak (A≈0.9956) can be achieved with **P** = [0.553 μm, 0.15 μm, 3.79 μm, 0.67 μm, 0.26 μm]. The corresponding spectra of the optimal GMCMG structure are present in the insert of Fig. 6. Obviously, an approximate perfect absorption peak (A≈0.9956)

appears in the absorption spectrum of this structure. That is to say, a perfect absorber can be obtained by using this GMCMG structure based on the excitation of SPPs mode on GNG and the inverse design technology. Comparing with existing perfect absorbers schemes based on graphene and black phosphorus [17–22,59,60], our structure can provide an absorption peak on the same level. Other than taking advantage of the characteristics of the GMCMG structure, the design scheme combining μ-GA enables us to further incorporate the influence of different structure parameter.
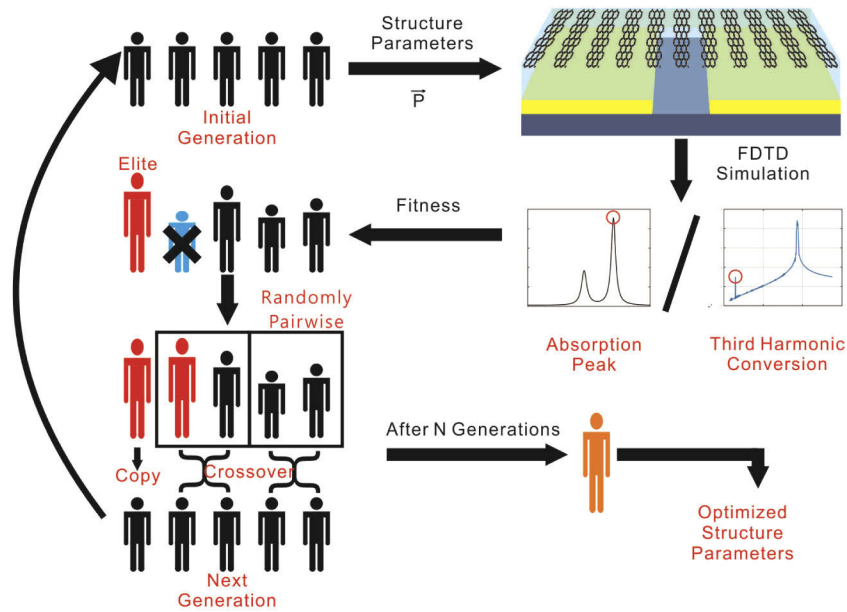

Fig. 5. Flowchart of an optimization process for the GMCMG by using the μ-GA.
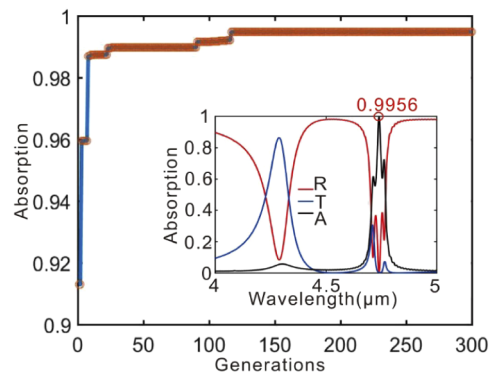

Fig. 6. Evolution of the absorption peak for the GMCMG structure in each generation. Red dots represent the simulated absorption peaks in each generation. The blue solid line is the connection of the red dots. The insert is the corresponding transmission (T), reflection (R), absorption (A) spectra of the optimal GMCMG structure optimized by using the μ-GA. The absorption peak of the point marked by the red circle in the absorption spectrum is 0.9956.

3.2. Third harmonic generation

It has been demonstrated that the graphene has a strong third-order nonlinear capability [61]. The third harmonic nonlinear response of the graphene can be described by the nonlinear conductivity coefficient defined as [62]:

$$\sigma_3(\omega) = j\frac{3}{32}\frac{e^2}{\pi\hbar^2}\frac{(ev_F)^2}{\mu_c\omega^3} \tag{8}$$

where v_F (=9.5×10^5 m/s), ω and d (=0.34 nm) indicate the Fermi velocity, the fundamental frequency of pumping light and the thickness of the monolayer graphene, respectively. The nonlinear susceptibility of the graphene is calculated as [63]:

$$\chi^{(3)}(\omega) = \frac{\sigma_3(\omega)}{\omega d} \tag{9}$$

As described above, the GMCMG structure can significantly enhance the light-matter interaction in the graphene at a specific wavelength. Thus, the nonlinear CE of the GMCMG is expected to be improved at the wavelength where the perfect absorption occurs. However, in addition to the absorption rate of a certain wavelength, the phase-matching condition also affects the nonlinearity ability of the structure [62]. In order to integrate the influence of different factors in optimizing the nonlinear CE, the μ-GA is applied to help us optimize the design of the structure. The process of optimizing the CE of THG is similar to the process of optimizing the absorption peak described above, whose flowchart can also be seen in Fig. 5. In the optimization for the CE of THG, each individual requires two FDTD simulations. In the first FDTD simulation, the wavelength of the highest absorption peak is determined, at which light-matter interaction is enhanced substantially. In the second FDTD simulation, the structure is illuminated by normal-incidence light with the center wavelength at the absorption peak obtained in the first simulation. And its power density is 0.18 MW/cm^2, which is sufficient to stimulate considerable nonlinearity of the structure. The fitness of the μ-GA here is the CE of THG calculated in the second simulation, which can be expressed as:

$$\text{CE} = \frac{\int_0^{L_{per}} P_y^{TH} dx}{P_{FF}L_{per}} \tag{10}$$

where P_{FF} is the power density of the incidence light, P_y^{TH} is the y component of the Poynting vector at the third harmonic frequency. In other words, we expect to obtain the maximum value of the normalized light transmittance (NLT) of the transmitted light at 1/3 wavelength of the incident light based on our structure. And the NLT is calculated by normalizing the transmitted electromagnetic field power to that of the incident light at the fundamental frequency. We set the optimization spaces of structure parameters as D_1 (0.4 μm–0.7 μm), D_2 (0.05 μm–0.15 μm), L_{per} (3.6 μm–4.4 μm), D_{int} (0.2 μm–0.4 μm), L_{gap} (0.1 μm–0.3 μm). The initial best individual's CE of THG under this condition is −76.62 dB with **P** = [0.6 μm, 0.07 μm, 3.8 μm 0.24 μm, 0.21 μm]. The other four individuals in the initial generation are randomly generated from the optimization space. The evolution of the CE of THG for each generation is shown in Fig. 7. After 300 generations, the highest CE is −58.52 dB (1.406×10^{-6}) with **P** = [0.595 μm, 0.14 μm, 3.8 μm, 0.2 μm, 0.26 μm]. The NLT spectrum of the optimal structure is present in the insert of Fig. 7. The higher transmission peak in this figure is at the incident wavelength. And an apparent transmission peak whose height is −58.52 dB can be observed at the 1/3 wavelength of the incident light (1.54 μm). In other words, the CE of THG of the structure can reach −58.52 dB. Different from the traditional method to enhance nonlinear CE of structures by using phase matching between the fundamental mode and the third harmonic mode [64], our scheme adopts the enhanced interaction between nonlinear substance and light at specific wavelengths to achieve nonlinear enhancement. It needs lower requirements for phase-matching conditions, which makes

it easier to implement in practice [65]. Several nanostructures have been proposed for THG employing dielectric metasurface and graphene. In Ref. [66], the absolute CE of 1.2×10^{-6} with a pump intensity of 3.2 GW/cm^2 is achieved based on a silicon metasurface, a third-harmonic generation CE of 3.68×10^{-7} can be realized based on graphene-assisted structure with an incident power density of 0.19 MW/cm^2 in Ref. [65] and the CE of -59.2 dB (1.202×10^{-6}) has been achieved with pump incident 1.52 MW/cm^2 based on propagating SPPs waves on graphene sheets in Ref. [62]. Comparing with these reports, our proposed scheme can reach higher CE under a lower pump intensity.
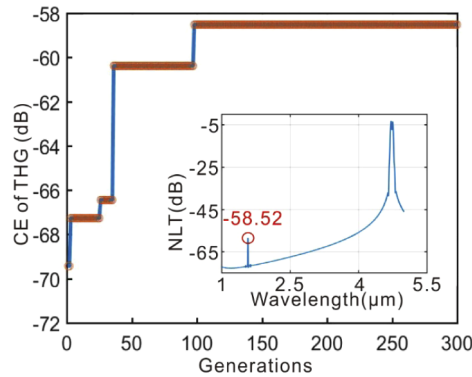

Fig. 7. Evolution of the CE of THG in each generation. Red dots represent the simulated CEs of THG in each generation. The blue solid line is the connection of the red dots. The insert is the NLT spectrum of the optimal GMCMG structure optimized by using the μ-GA. The NLT of the point marked by the red circle in the spectrum is -58.52 dB.

4. Conclusions

In this article, we propose three different nanostructures consist of graphene metamaterials coupling with metallic grating. With these structures, the PIR effects can be obtained based on the destructive interference between the SPPs modes excited on graphene and the hybrid modes in the nearby medium. The simulation results demonstrate the roles of the key structural parameters and chemical potential of graphene in regulating these PIR effects. In the proposed structures, the interaction between graphene and light passing through it is enhanced. Based on this, we can not only gain a perfect absorber but also optimize the CE of the THG for this structure. After the optimization with the μ-GA algorithm, a perfect absorber with an absorption peak of as high as 0.9956 and an efficient third harmonic generator, whose absolute CE of THG reaches 1.406×10^{-6} with a peak pump intensity as low as 0.18 MW/cm^2, are achieved. Based on these two outstanding optical properties, some interesting applications can be developed in sensors, absorbers, switching and so on.

Disclosures

The authors declare that there are no conflicts of interest related to this article.

References

1. F. Schwierz, "Graphene transistors," Nat. Nanotechnol. **5**(7), 487–496 (2010).
2. A. N. Grigorenko, M. Polini, and K. S. Novoselov, "Graphene plasmonics," Nat. Photonics **6**(11), 749–758 (2012).
3. L. Wang, S. Ge, W. Hu, M. Nakajima, and Y. Lu, "Graphene-assisted high-efficiency liquid crystal tunable terahertz metamaterial absorber," Opt. Express **25**(20), 23873–23879 (2017).
4. X. He, X. Zhong, F. Lin, and W. Shi, "Investigation of graphene assisted tunable terahertz metamaterials absorber," Opt. Mater. Express **6**(2), 331–342 (2016).
5. N. Kumar, J. Kumar, C. Gerstenkorn, R. Wang, H.-Y. Chiu, A. L. Smirl, and H. Zhao, "Third harmonic generation in graphene and few-layer graphite films," Phys. Rev. B **87**(12), 121406 (2013).
6. S.-Y. Hong, J. I. Dadap, N. Petrone, P.-C. Yeh, J. Hone, and R. M. Osgood Jr, "Optical third-harmonic generation in graphene," Phys. Rev. X **3**(2), 021014 (2013).
7. S. A. Mikhailov and K. Ziegler, "Nonlinear electromagnetic response of graphene: frequency multiplication and the self-consistent-field effects," J. Phys.: Condens. Matter **20**(38), 384204 (2008).
8. M. M. Glazov, "Second harmonic generation in graphene," JETP Lett. **93**(7), 366–371 (2011).
9. T. Guo, B. Jin, and C. Argyropoulos, "Hybrid graphene-plasmonic gratings to achieve enhanced nonlinear effects at terahertz frequencies," Phys. Rev. Appl. **11**(2), 024050 (2019).
10. R. R. Nair, P. Blake, A. N. Grigorenko, K. S. Novoselov, T. J. Booth, T. Stauber, N. M. R. Peres, and A. K. Geim, "Fine structure constant defines visual transparency of graphene," Science **320**(5881), 1308 (2008).
11. S. Yan, X. Zhu, L. H. Frandsen, S. Xiao, N. A. Mortensen, J. Dong, and Y. Ding, "Slow-light-enhanced energy efficiency for graphene microheaters on silicon photonic crystal waveguides," Nat. Commun. **8**(1), 1–8 (2017).
12. T. Zhang, J. Dai, Y. Dai, Y. Fan, X. Han, J. Li, F. Yin, Y. Zhou, and K. Xu, "Tunable plasmon induced transparency in a metallodielectric grating coupled with graphene metamaterials," J. Lightwave Technol. **35**(23), 5142–5149 (2017).
13. Z. Fang, Y. Wang, A. E. Schlather, Z. Liu, P. M. Ajayan, F. J. G. de Abajo, P. Nordlander, X. Zhu, and N. J. Halas, "Active tunable absorption enhancement with graphene nanodisk arrays," Nano Lett. **14**(1), 299–304 (2014).
14. X. Gan, K. F. Mak, Y. Gao, Y. You, F. Hatami, J. Hone, T. F. Heinz, and D. Englund, "Strong enhancement of light–matter interaction in graphene coupled to a photonic crystal nanocavity," Nano Lett. **12**(11), 5626–5631 (2012).
15. T. Zhang, J. Dai, Y. Dai, Y. Fan, X. Han, J. Li, F. Yin, Y. Zhou, and K. Xu, "Dynamically tunable plasmon induced absorption in graphene-assisted metallodielectric grating," Opt. Express **25**(21), 26221–26233 (2017).
16. J. S. Gomez-Diaz, M. Tymchenko, and A. Alù, "Hyperbolic metasurfaces: surface plasmons, light-matter interactions, and physical implementation using graphene strips," Opt. Mater. Express **5**(10), 2313–2329 (2015).
17. Y. Long, Y. Li, L. Shen, W. Liang, H. Deng, and H. Xu, "Dually guided-mode-resonant graphene perfect absorbers with narrow bandwidth for sensors," J. Phys. D **49**(32), 32LT01 (2016).
18. M. Grande, M. A. Vincenti, T. Stomeo, G. V. Bianco, D. De Ceglia, N. Aközbek, V. Petruzzelli, G. Bruno, M. De Vittorio, M. Scalora, and A. D'Orazio, "Graphene-based absorber exploiting guided mode resonances in one-dimensional gratings," Opt. Express **22**(25), 31511–31519 (2014).
19. M. Grande, M. A. Vincenti, T. Stomeo, G. V. Bianco, D. De Ceglia, N. Aközbek, V. Petruzzelli, G. Bruno, M. De Vittorio, M. Scalora, and A. D'Orazio, "Graphene-based perfect optical absorbers harnessing guided mode resonances," Opt. Express **23**(16), 21032–21042 (2015).
20. Y. L. Liao and Y. Zhao, "Graphene-based tunable ultra-narrowband mid-infrared TE-polarization absorber," Opt. Express **25**(25), 32080–32089 (2017).
21. A. Akhavan, S. Abdolhosseini, H. Ghafoorifard, and H. Habibiyan, "Narrow band total absorber at near-infrared wavelengths using monolayer graphene and sub-wavelength grating based on critical coupling," J. Light. Technol. **36**(23), 5593–5599 (2018).
22. X. Jia, X. Wang, C. Yuan, Q. Meng, and Z. Zhou, "Novel dynamic tuning of broadband visible metamaterial perfect absorber using graphene," J. Appl. Phys. **120**(3), 033101 (2016).
23. Y. M. Qing, H. F. Ma, S. Yu, and T. J. Cui, "Tunable dual-band perfect metamaterial absorber based on a graphene-SiC hybrid system by multiple resonance modes," J. Phys. D: Appl. Phys. **52**(1), 015104 (2019).
24. S. Molesky, Z. Lin, A. Y. Piggott, W. Jin, J. Vucković, and A. W. Rodriguez, "Inverse design in nanophotonics," Nat. Photonics **12**(11), 659–670 (2018).
25. B. Vial and Y. Hao, "Topology optimized all-dielectric cloak: design, performances and modal picture of the invisibility effect," Opt. Express **23**(18), 23551–23560 (2015).
26. T. Zhang, J. Wang, Y. Dan, Y. Lanqiu, J. Dai, X. Han, X. Sun, and K. Xu, "Efficient training and design of photonic neural network through neuroevolution," Opt. Express **27**(26), 37150–37163 (2019).
27. J. Peurifoy, Y. Shen, L. Jing, Y. Yang, F. Cano-Renteria, B. G. DeLacy, J. D. Joannopoulos, M. Tegmark, and M. Soljačić, "Nanophotonic particle simulation and inverse design using artificial neural networks," Sci. Adv. **4**(6), eaar4206 (2018).
28. T. Zhang, J. Wang, Q. Liu, J. Zhou, J. Dai, X. Han, Y. Zhou, and K. Xu, "Efficient spectrum prediction and inverse design for plasmonic waveguide systems based on artificial neural networks," Photonics Res. **7**(3), 368–380 (2019).

29. T. W. Hughes, M. Minkov, I. A. D. Williamson, and S. Fan, "Adjoint method and inverse design for nonlinear nanophotonic devices," ACS Photonics **5**(12), 4781–4787 (2018).

30. M. A. Swillam, M. H. Bakr, and X. Li, "Accurate sensitivity analysis of photonic devices that exploit the finite-difference time-domain central adjoint variable method," Appl. Opt. **46**(9), 1492–1499 (2007).

31. S. Jafar-Zanjani, S. Inampudi, and H. Mosallaei, "Adaptive genetic algorithm for optical metasurfaces design," Sci. Rep. **8**(1), 11040–16 (2018).

32. Y. Zhang, S. Yang, A. E.-J. Lim, G.-Q. Lo, C. Galland, T. Baehr-Jones, and M. Hochberg, "A compact and low loss Y-junction for submicron silicon waveguide," Opt. Express **21**(1), 1310–1316 (2013).

33. Z. Yu, H. Cui, and X. Sun, "Genetic-algorithm-optimized wideband on-chip polarization rotator with an ultrasmall footprint," Opt. Lett. **42**(16), 3093–3096 (2017).

34. Y. Tang, J. A. Bossard, D. H. Werner, and T. S. Mayer, "Single-layer metallodielectric nanostructures as dual-band midinfrared filters," Appl. Phys. Lett. **92**(26), 263106 (2008).

35. P.-H. Fu, S.-C. Lo, P.-C. Tsai, K.-L. Lee, and P.-K. Wei, "Optimization for gold nanostructure-based surface plasmon biosensors using a microgenetic algorithm," ACS Photonics **5**(6), 2320–2327 (2018).

36. S. Chakravarty, R. Mittra, and N. R. Williams, "Application of a microgenetic algorithm (MGA) to the design of broadband microwave absorbers using multiple frequency selective surface screens buried in dielectrics," IEEE Trans. Antennas Propag. **50**(3), 284–296 (2002).

37. K. Krishnakumar, "Micro-genetic algorithms for stationary and non-stationary function optimization," Proc. SPIE **1196**, 289–296 (1990).

38. T. Huang and A. S. Mohan, "Micro-particle swarm optimizer for solving high dimensional optimization problems (μPSO for high dimensional optimization problems)," Appl. Math. Comput. **181**(2), 1148–1154 (2006).

39. H. Salehinejad, S. Rahnamayan, and H. R. Tizhoosh, "Micro-differential evolution: Diversity enhancement and a comparative study," Appl. Soft Comput. **52**, 812–833 (2017).

40. Z. Li, D. Rosenmann, D. A. Czaplewski, X. Yang, and J. Gao, "Strong circular dichroism in chiral plasmonic metasurfaces optimized by micro-genetic algorithm," Opt. Express **27**(20), 28313–28323 (2019).

41. Z. Li, L. Stan, D. A. Czaplewski, X. Yang, and J. Gao, "Broadband infrared binary-pattern metasurface absorbers with micro-genetic algorithm optimization," Opt. Lett. **44**(1), 114–117 (2019).

42. M. Janfaza, M. A. Mansouri-Birjandi, and A. Tavousi, "Dynamic switching between single and double plasmon induced reflection through graphene nanoribbons based structure," Mater. Res. Express **5**(11), 115022 (2018).

43. S.-X. Xia, X. Zhai, L.-L. Wang, and S.-C. Wen, "Plasmonically induced transparency in double-layered graphene nanoribbons," Photonics Res. **6**(7), 692–702 (2018).

44. Z. Liu, E. Gao, Z. Zhang, H. Li, H. Xu, X. Zhang, X. Luo, and F. Zhou, "Dual-mode on-to-off modulation of plasmon-induced transparency and coupling effect in patterned graphene-based terahertz metasurface," Nanoscale Res. Lett. **15**(1), 1–9 (2020).

45. D. Chun-Feng, Z. Ya-Ting, Y. Jian-Quan, S. Chong-Ling, X. De-Gang, and Z. Gui-Zhong, "Reflection-type electromagnetically induced transparency analogue in terahertz metamaterials," Chin. Phys. B **23**(12), 124203 (2014).

46. H.-J. Li, X. Zhai, and L.-L. Wang, "Realizing controlled plasmonically induced reflection in metal–insulator–metal plasmonic waveguide-resonator coupling systems," Appl. Phys. Express **8**(9), 092201 (2015).

47. G. W. Hanson, "Dyadic Green's functions and guided surface waves for a surface conductivity model of graphene," J. Appl. Phys. **103**(6), 064302 (2008).

48. T. Zhang, L. Chen, and X. Li, "Graphene-based tunable broadband hyperlens for far-field subdiffraction imaging at mid-infrared frequencies," Opt. Express **21**(18), 20888–20899 (2013).

49. E. Sakat, G. Vincent, P. Ghenuche, N. Bardou, S. Collin, F. Pardo, J. L. Pelouard, and R. Haïdar, "Guided mode resonance in subwavelength metallodielectric free-standing grating for bandpass filtering," Opt. Lett. **36**(16), 3054–3056 (2011).

50. L. Ju, B. Geng, J. Horng, C. Girit, M. Martin, Z. Hao, H. A. Bechtel, X. Liang, A. Zettl, Y. R. Shen, and F. wang, "Graphene plasmonics for tunable terahertz metamaterials," Nat. Nanotechnol. **6**(10), 630–634 (2011).

51. S. F. Mingaleev, A. E. Miroshnichenko, and Y. S. Kivshar, "Coupled-resonator-induced reflection in photonic-crystal waveguide structures," Opt. Express **16**(15), 11647–11659 (2008).

52. X. He, Y. Yao, Y. Huang, Q. Zhang, L. Zhu, F. Wu, G. Ying, and J. Jiang, "Active manipulation of electromagnetically induced reflection in complementary terahertz graphene metamaterial," Opt. Commun. **407**, 386–391 (2018).

53. S. Shen, Y. Liu, W. Liu, Q. Tan, J. Xiong, and W. Zhang, "Tunable electromagnetically induced reflection with a high Q factor in complementary Dirac semimetal metamaterials," Mater. Res. Express. **5**(12), 125804 (2018).

54. Y. Liang, W. Peng, R. Hu, and L. Xie, "Extraordinary optical properties in the subwavelength metallodielectric free-standing grating," Opt. Express **22**(16), 19484–19494 (2014).

55. H.-S. Chu and C. How Gan, "Active plasmonic switching at mid-infrared wavelengths with graphene ribbon arrays," Appl. Phys. Lett. **102**(23), 231107 (2013).

56. X. Han, T. Wang, X. Li, S. Xiao, and Y. Zhu, "Dynamically tunable plasmon induced transparency in a graphene-based nanoribbon waveguide coupled with graphene rectangular resonators structure on sapphire substrate," Opt. Express **23**(25), 31945–31955 (2015).

57. R. Yu, R. Alaee, F. Lederer, and C. Rockstuhl, "Manipulating the interaction between localized and delocalized surface plasmon-polaritons in graphene," Phys. Rev. B **90**(8), 085409 (2014).

58. D. E. Goldenberg, "*Genetic algorithms in search, optimization and machine learning*," (Addison Wesley, Reading: MA, 1989).

59. S.-X. Xia, X. Zhai, Y. Huang, J.-Q. Liu, L.-L. Wang, and S.-C. Wen, "Multi-band perfect plasmonic absorptions using rectangular graphene gratings," Opt. Lett. **42**(15), 3052–3055 (2017).

60. S.-X. Xia, X. Zhai, L.-L. Wang, and S.-C. Wen, "Polarization-independent plasmonic absorption in stacked anisotropic 2D material nanostructures," Opt. Lett. **45**(1), 93–96 (2020).

61. M. R. Shcherbakov, D. N. Neshev, B. Hopkins, A. S. Shorokhov, I. Staude, E. V. Melik-Gaykazyan, M. Decker, A. A. Ezhov, A. E. Miroshnichenko, I. Brener, A. A. Fedyanin, and Y. S. Kivshar, "Enhanced third-harmonic generation in silicon nanoparticles driven by magnetic response," Nano Lett. **14**(11), 6488–6492 (2014).

62. H. Nasari and M. S. Abrishamian, "Quasi-phase matching for efficient long-range plasmonic third-harmonic generation via graphene," Opt. Lett. **40**(23), 5510–5513 (2015).

63. T. Gu, N. Petrone, J. F. McMillan, A. van der Zande, M. Yu, G. Q. Lo, D. L. Kwong, J. Hone, and C. W. Wong, "Regenerative oscillation and four-wave mixing in graphene optoelectronics," Nat. Photonics **6**(8), 554–559 (2012).

64. P. Navaeipour, I. Al-Naib, and M. M. Dignam, "Third Harmonic THz Generation from Graphene in a Parallel-Plate Waveguide," arXiv preprint arXiv:1710.04075 (2017).

65. J. Li, T. Zhang, and L. Chen, "High-efficiency plasmonic third-harmonic generation with graphene on a silicon diffractive grating in mid-infrared region," Nanoscale Res. Lett. **13**(1), 338 (2018).

66. Y. Yang, W. Wang, A. Boulesbaa, I. I. Kravchenko, D. P. Briggs, A. Puretzky, D. Geohegan, and J. Valentine, "Nonlinear Fano-resonant dielectric metasurfaces," Nano Lett. **15**(11), 7388–7393 (2015).